Acta Astronautica 226 (2025) 611–625

Contents lists available at ScienceDirect

Acta Astronautica

journal homepage: www.elsevier.com/locate/actaastro

Research paper

Synthetic thermal image generation and processing for close proximity operations

Lucia Bianchi *, Michele Bechini, Matteo Quirino, Michèle Lavagna

Department of Aerospace Science and Technology, Politecnico di Milano, via La Masa 34, Milano, 20156, Italy

ARTICLE INFO

Keywords:
Spacecraft thermal infrared imaging
Earth thermal infrared imaging
Thermal image generation
Region of interest detection

ABSTRACT

The new scenarios foreseen in forthcoming space missions have increased interest towards optical-based relative navigation techniques, which have demonstrated efficacy in a variety of operational conditions. Although object detection methods have predominantly been used within the visible spectrum, optical payloads struggle in weak lighting conditions and are susceptible to overexposure. Consequently, thermal imaging systems are being investigated as a potential solution, as their integration into the current systems would greatly extend future mission capabilities. This study seeks to fill the gap in literature by assessing the performance of state-of-the-art object detection algorithms with images captured in the thermal spectrum. Given the scarcity of readily available thermal infrared (TIR) images captured in orbit, a novel rendering pipeline is implemented to generate physically accurate thermal images relevant to close-proximity scenarios. These synthetic representations feature a simplified target spacecraft against Earth and deep space backgrounds, including variations in illumination conditions, material properties, relative state, and scale. To ensure realistic outputs, the radiative field of the Earth is modelled based on satellite measurements collected in the cloud and Earth radiant energy system (CERES) database. To enrich the fidelity of the outputs, a thermal sensor model and the corresponding noise levels are introduced in the pipeline. The generated images are then used to test the performance of traditional object detection algorithms in discerning the region of interest (ROI) under different orbital scenarios. The results demonstrate the effectiveness of the selected methodologies in mitigating the influence of the Earth in the ROI extraction process, while also revealing a performance degradation due to the presence of multi-material targets.

1. Introduction

In recent years, the use of optical navigation for relative maneuvers has grown in interest within the scientific community, and various methodologies have been proposed to address close-proximity operations around cooperative or uncooperative targets, whether celestial or artificial in nature.

In this context, the development of a robust and accurate guidance, navigation and control procedure that can be executed on-board in real-time is crucial to ensure successful operations and guarantee the correct interaction within objects in space. With the current trend towards autonomous on-board activities, this requirement translates into the capability of the chaser spacecraft to reconstruct the surrounding scene and recover the relative pose with respect to the observed mission target. Consequently, cameras and optical sensors are commonly employed, providing high-frequency measurements crucial for performing fast actions, especially in unknown environments [1]. Traditionally, monocular visible cameras have found widespread applications in close-range mission scenarios, due to their mass and power-effectiveness [2], demonstrating high performance in recovering the relative state [3–5]. However, these sensors face significant limitations related to illumination conditions, which strongly impact the overall robustness and accuracy of the measurements [4,6]. A promising solution proposed in recent years is the use of TIR imaging [7,8], which enables the discrimination of scene objects based on their temperature distribution rather than their ability to reflect light. Their use would thereby introduce notable advantages from a navigation perspective, allowing for the detection of the spacecraft or other objects even in shadow conditions.

To demonstrate the applicability of monocular thermal images to autonomous relative navigation tasks, this work presents a comprehensive insight into the performance attainable with ROI detection algorithms when applied to noisy thermal images of spaceborne scenarios. Given the limited availability of in-flight infrared images and validated virtual TIR datasets, a collection of synthetic images is generated starting from the work proposed in [9–11]. To further stress the performance of image processing algorithms, the generated images include

* Corresponding author.
E-mail address: lucia.bianchi@polimi.it (L. Bianchi).

https://doi.org/10.1016/j.actaastro.2024.10.061
Received 26 June 2024; Received in revised form 9 October 2024; Accepted 24 October 2024
Available online 4 November 2024

List of Acronyms

A/D	analog to digital
ADU	analog to digital unit
CERES	cloud and Earth radiant energy system
DoG	difference of gaussian
IoU	intersection over union
NVD	noise voltage density
RMS	root mean square
ROI	region of interest
SYN	synoptic TOA and surface fluxes and clouds
TIR	thermal infrared
TOA	top of the atmosphere
VIS	visible
WGE	weak gradient elimination

the Earth as background disturbance, demonstrating their possible application to low-Earth close-proximity scenarios. Unlike the 3D thermal finite volume model used for the thermal characterization of the artificial target [9,12], the infrared properties of the Earth and its atmosphere are modelled according to the satellite-based measurements collected in the CERES database [13].

The main contributions proposed by this work can be summarized as:

- Definition of an analytical thermal camera model to replicate the instrument response to an external radiating source, including the modelling of the main noise sources.
- Introduction of the Earth into the generated synthetic images, as additional disturbance for the image processing algorithms, where the thermal properties of the Earth and its atmosphere are modelled according to the satellite-based measurements collected in the CERES database [13].
- Evaluation of the performance of state-of-the-art image processing techniques with the purpose of ROI detection tasks when only monocular thermal images are available.

The remainder of the paper is organized as follows: Section 2 provides an overview of the applications of TIR imaging for space purposes, including a brief overview of the methodologies used to generate synthetic thermal images, the datasets already publicly available, and a review of the literature regarding object detection in space. The implemented camera model is presented in Section 3, which includes the modelling of main disturbance sources and the infrared representation of the Earth. Section 4 presents the results achieved by state-of-the-art computer vision methodologies when applied to a simplified spacecraft geometry, while Section 5 extends the discussion to the applicative case of Tango satellite [14]. Finally, Section 6 summarizes the conclusions and main outcomes of this work, while also suggesting possible future developments.

2. Related works

Thermal cameras are widely used for remote sensing activities, such as investigating the physico-chemical composition of planetary surfaces and assessing the landing site for a safe descent trajectory. In recent years, TIR sensors have also been exploited for GNC purposes, as demonstrated by the Japanese Hayabusa2 mission [15], which employed artificial markers on the Ryugu asteroid surface for autonomous landing. More recently, thermal sensors have been flight-tested during non-cooperative rendezvous as part of the LIRIS demonstrator onboard the ATV5 Mission [16], as well as in tracking activities as part of the Raven ISS Hosted Payload [17]. The potential of the TIR cameras in the context of relative navigation has been investigated by [7], demonstrating the potential of using SLAM-based approach with thermal images, yet highlighting the necessity of more realistic TIR space imagery to further evaluate these methods.

In the context of navigation tasks, it is important to pre-process the input images to enhance the image quality and extract the ROI corresponding to the target under analysis, which is crucial when dealing with complex backgrounds [3,18]. A feature-based approach called weak gradient elimination (WGE) has been developed and introduced by [4] as part of the Sharma-Ventura-D'Amico (SVD) architecture for monocular vision-based navigation. It is specifically design to distinguish between the target and the background in visible (VIS) images by leveraging the assumption that the Earth, or the generic background disturbance, has a lower gradient compared to the foreground elements, which typically have sharp edges, thus higher gradients. Despite the high performance, this method faces challenges when the target overlaps the Earth terminator or when there is a limited contrast between the foreground and background of the image [4]. An alternative formulation to the WGE has been proposed by [19], where the choice of ROI extraction algorithms depends on the particular scenario presented in the image. If the Earth is within the FOV of the camera, WGE is applied to discriminate the target against the complex background; in scenarios with a deep space background, the simpler and computationally inexpensive Otsu thresholding is applied. While this approach appears to be more robust that using WGE alone, it does not directly address the limitations identified for the WGE. More recently, CNN-based approaches have been used to extract the ROI with different backgrounds, demonstrating improved performance with respect to classical methods. [20] employed a novel CNN architecture to detect the target in images with various backgrounds, introducing also a novel training approach to improve the robustness of the architecture when trained only on synthetic images. While the literature provides a large scale of applicative studies of ROI extraction process in the field of VIS imaging in space scenarios, few examples can be found regarding thermal images due to the limited availability of representations. The filtering-like technique presented by [4] has been tested on a small dataset of both TIR and VIS-TIR fused images in [21], but the presented work lacks detailed ROI detection performance analysis. As alternative, an enhanced gradient descent method to extract the foreground target from complex backgrounds has been proposed by [22], where thermal images of the ISS are used as a test case. This approach combines the detection capabilities of difference of gaussian (DoG) filter technique with graph manifold ranking based on foreground saliency generation, reaching performance comparable with traditional state-of-the art methodologies. Additionally, CNN-based architectures have been preliminary tested on TIR imaging, as presented in [23]. Although this work hinges on developing a pose-estimation pipeline for VIS imaging, the network has been trained on MINIMA images [6] and tested on a small set of TIR and VIS-TIR fused images, demonstrating the adaptability of the pipeline in accurately extract the ROI also from images captured in the thermal spectrum.

The lack of in-flight thermal images has driven the need to create and leverage synthetic TIR images that reflect space scenarios. [24] propose a pipeline for generating a set of infrared images acquired in a laboratory facility using a thermal mock-up, highlighting the challenges of the acquisition process, particularly in replicating the thermal characteristics of the target and incorporating the Earth as background disturbance. An alternative approach to generate thermal images involves the use of rendering software. A VIS-TIR images collection is proposed in [25], where synthetic images of ENVISAT with deep space background are created using the ASTOS Camera Simulator. However, these representations are not publicly available, and the solid background of the presented images poses little challenges to the detection algorithms. Another dataset is proposed by [26], featuring open-source multispectral images of space debris generated using Vega Prime

Software and MODIS atmospheric tool to accurately define hourly-dependent temperature distributions across different spectral bands. As these images are representative also of low-Earth dynamical environments, the background includes portions of the Earth, characterized using images from the Himawari-8 weather satellite [27]. Despite their potential for testing the performance of object detection algorithms, the presented datasets highlight several drawbacks, including unavailability, lack of realistic representations, and absence of annotations useful for navigation purposes. These limitations, combined with the need for a flexible tool to simulate various of mission scenarios and potentially implement GNC algorithms based on TIR images, justify the effort to develop a dedicated synthetic image simulator.

3. Thermal image modelling

To improve the fidelity of the generated images and replicate the digital output of the sensor, the analytical model of a thermal camera is introduced in the rendering pipeline. The following sections detail the analytical formulation implemented to model the behaviour of a TIR imager, along with its primary noise sources and their effect on the final representations. Furthermore, to include an additional level of disturbance to the rendered images, the Earth is included in the background. Hence, this section also provides the reader with an introduction to the modelling of the infrared behaviour of the Earth. Lastly, a brief overview of the rendering sequence used to generate the final synthetic TIR images is provided.

3.1. Thermal camera model

In literature, infrared sensors are commonly classified into two main families: photon detectors and thermal detectors [28]. The former category absorbs the incident photons leading to a change in the concentration of free charge carriers, hence modifying the overall electrical energy. Instead, thermal detectors are transducers in which the incident radiation is first converted into thermal energy, and then the electrical output is generated from a change in a physical property of the detector material. For a detailed comparative analysis, the reader can refer to [28,29]. Despite their limited measurement precision, in the past few years thermal detectors have proved interesting for space applications, as robust, lightweight and inexpensive thermal cameras. Within this category, uncooled microbolometers have already been widely tested in missions around Earth and towards inner Solar System planets, such as Rosetta [30], Bepi-Colombo [31] and Hayabusa2 [15]. Since the electric signal generated by the sensor is proportional to the radiation of the observed object, the first step in modelling the instrument involves the characterization of the radiative properties of the object under analysis. Leveraging the fundamental radiometric principles, the intensity of emitted radiation can be expressed in $\mathrm{W\,m^{-2}\,sr^{-1}}$ as shown in Eq. (1) [32]:

$$i = \int_0^\infty \varepsilon(\lambda) B(\lambda, T) d\lambda \tag{1}$$

Where λ is the wavelength, $B(\lambda, T)$ is the monochromatic radiation expressed by the Planck's law, and $\varepsilon(\lambda)$ and T are the monochromatic diffuse emissivity and the temperature of the observed object, respectively. Assuming the observed target is a Lambertian emitter, i.e., it radiates uniformly in all directions, the radiant flux emitted towards the camera is quantified by introducing the view factor between the sensor and the object. Following the procedure proposed in [9,10], the heat flux per unit area from the object face to the sensor lens is expressed by Eq. (2), where $\hat{\mathbf{n}}_f$ is the normal vector to the mesh element, $\hat{\mathbf{n}}_s$ is the normal vector to the sensor lens, $\mathbf{r}_{fs}$ is the distance vector from the mesh element to the sensor plane, and ΔA_c is the sensor area intercepting the radiation.

$$q_{fs} = i \, \frac{(\hat{\mathbf{n}}_f \cdot \mathbf{r}_{fs})(\hat{\mathbf{n}}_s \cdot \mathbf{r}_{sf})}{|\mathbf{r}_{fs}|^4} \Delta A_c \tag{2}$$

In general applications, the sensor performance is influenced by the presence of atmosphere and the surrounding environment, resulting in the attenuation of the received signal. However, in space applications, the absence of a stable atmosphere and the near-zero temperature of deep space lead to the assumption that the heat flux per unit area reaching the sensor lens coincides with the flux emitted by the object towards the camera. Hence, no environmental attenuations are considered in the model.

Before reaching the detector of the instrument, where the radiation is converted into electrical input, the thermal signal passes through a series of lenses and filters, designed to enhance the sensitivity of the sensor [28]. The presence of these optical components may introduce non-trivial drawbacks, including the absorption and reflection of a fraction of the incoming radiation, thereby reducing the overall signal transmission. This effect is crucial for accurately representing the behaviour of the thermal sensor, and is therefore encompassed into the model through the camera response function defined in Eq. (3) [33,34]. This spectral curve depends on the camera detection efficiency η, lens transparency $R_{\mathcal{L}}(\lambda)$ and transmittance of the band-pass filter $R_{\mathcal{F}}(\lambda)$, respectively.

$$R(\lambda) = \eta R_{\mathcal{L}}(\lambda) R_{\mathcal{F}}(\lambda) \tag{3}$$

The analytical expression of $R(\lambda)$, derived from the analyses of the Hayabusa2 data presented in [33], is described through skewed bell-shaped curves, and a visual comparison with the original data is presented in Fig. 1.

Finally, to compute the actual heat flux emitted from the object and intercepted by the sensing element of the camera, Eq. (3) is incorporated in Eq. (2) and the resulting expression is integrated over the entire frequency spectrum:

$$q_{fc} = \int_0^\infty \varepsilon(\lambda) B(\lambda, T) R(\lambda) d\lambda \, \frac{(\hat{\mathbf{n}}_f \cdot \mathbf{r}_{fs})(\hat{\mathbf{n}}_s \cdot \mathbf{r}_{sf})}{|\mathbf{r}_{fs}|^4} \Delta A_c \tag{4}$$

Once the radiation is recorded by the pixel array, an output voltage is generated, which is then amplified and converted into a digital bit string by an analog to digital (A/D) converter. Depending on the mission objectives, the microbolometer output may be expressed as function of either the radiant power emitted by the observed object or the heat flux intercepted by the detector.

Radiometry mode. For missions requiring a thermal characterization of the target, the digital output of the sensor in analog to digital unit (ADU) is defined as the linear dependency expressed by Eq. (5) [34,35]:

$$DN = a \cdot F(T) + b \tag{5}$$

Where a and b are the system response parameter, camera gain and camera offset respectively, recovered through radiometric calibration, and $F(T)$ is the emissive power described by [34]:

$$F(T) = \pi \int_0^\infty \varepsilon(\lambda) B(\lambda, T) R(\lambda) d\lambda \tag{6}$$

From the knowledge of the heat flux reaching the sensing element, $F(T)$ can be rewritten as function of the detected radiation by introducing a distance compensation factor $\mathcal{D}$, which depends on the mean distance between the camera and the geometrical center of the object.

$$F(T) = \mathcal{D} \, q_{fc} = \frac{\pi |\mathbf{r}_{fs}|^2}{\Delta A_c} q_{fc} \tag{7}$$

Once the digital response of the sensor is known, Eq. (5) is used to reconstruct the radiant temperature field of the observed object:

$$T_{rad} = \left(\frac{DN - b}{a\sigma} \right)^{1/4} \tag{8}$$

Note that the actual temperature distribution can be recovered by accounting for the emission spectrum of the object.

Detection mode. Under the assumption that the primary objective of the chaser spacecraft is exclusively to detect the presence of the object without acquiring any radiometric measurement, the introduction of

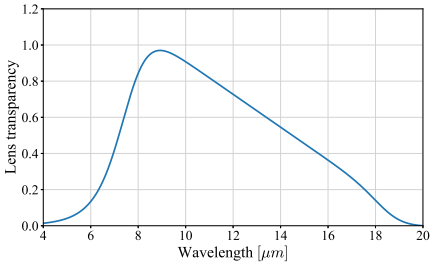

(a) Derived lens transparency.

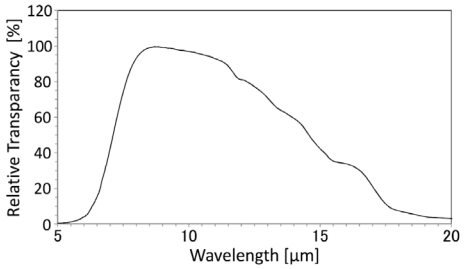

(b) Transparency of Hayabusa2 camera lenses [33].

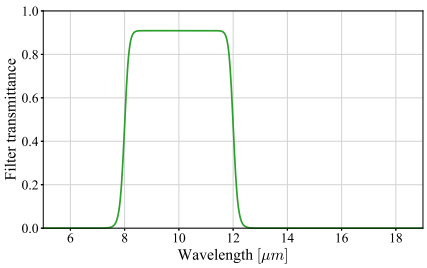

(c) Derived filter transmittance.

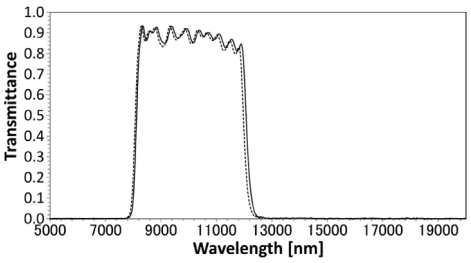

(d) Transmittance of Hayabusa2 camera filter [33].

Fig. 1. Camera response function: comparison of the derived model (left) with the Hayabusa2 data (rigth) [33].

the compensation parameter becomes unnecessary. In detection mode, the fundamental requirement is the presence of sufficient contrast between the observed object and the scene background, enabling a clear discrimination of the former with respect to the latter. In this context, the sensor output response in ADU can be defined as function of the detected radiation:

$$DN = a \cdot q_{fc}(T) + b \tag{9}$$

Note that in relative navigation scenarios, due to the absence of apriori knowledge of the camera-target distance, the camera must be operated in detection mode.

3.2. Earth thermal model

The majority of artificial objects orbit around the Earth, leading to the necessity of analysing the performance of object detection algorithms when this body falls within the background of the images. One of the simplest approach to incorporate the Earth into these representations involves the use of TIR images captured by real orbiting satellite systems [27]; however, the use of such representations is limited by the availability and lack of radiometric information included into the image. Indeed, an actual radiance scale of the Earth radiation budget is necessary to establish a correlation between the foreground and background layers of the image, thus knowledge of the Earth's thermal dynamics is pivotal. Rather than implementing a novel analytical framework to describe the radiation of the Earth and its atmosphere, satellite-based measurements collected in the CERES database [13] are exploited. The choice of such tool not only avoids the resource-intensive demands associated with thermal simulations, both in terms of development time and computational cost, but could also aids in improving the accuracy and precision of the outputs compared to those produced by the analytical model [36]. The following sections provide a brief introduction to the database and the steps implemented to transition from the original library data to the final radiometric information required for the image generation. Please note that the proposed methodology has been tailored for applications involving the Earth, but it can also be extended to other celestial body, provided that radiometric data are available, which may be sourced from a dedicated dataset or obtained through detailed thermal simulations.

3.2.1. CERES database

The CERES project has been designed to deliver satellite-based observations of the Earth's radiation budget, enabling the monitoring of the radiance variations on a temporal basis that spans monthly, weekly, daily or even hourly intervals. These data, collected via a suite of instruments aboard Earth observation satellites encompass incoming and out-coming solar radiation, as well as radiation emitted by the Earth surface, covering both the shortwave infrared and longwave infrared bands. The CERES scientific measurements are categorized into four primary classes: energy balanced and filled dataset, synoptic TOA and surface fluxes and clouds (SYN) library, single scanner footprint dataset, and fast longwave and shortwave flux library. For the purpose of this work, the SYN1deg collection is selected, which presents daily average all-sky fluxes with a 1° spatial resolution along both geographical coordinates. This product offers interpolated TOA fluxes achieved through cross calibration between geostationary imagers and MODIS imager measurements, alongside corresponding cloud properties. To include an extensive characterization of the atmospheric gas properties, these measurements are paired with specific fluxes derived through the implementation of the Fu-Liou radiative transfer model [37].

3.2.2. Temperature field computation

As discussed in more detail in Section 3.1, to accurately model the characteristics of the thermal instrument, the temperature field of the observed scene needs to be computed using Eq. (4). Assuming the Earth behaves as a blackbody, the equivalent temperature profile for each gridded location is computed using the Stefan Boltzmann's law [28]:

$$T = \left(\frac{F_E}{\sigma}\right)^{1/4} \tag{10}$$

Where σ is the Stefan–Boltzmann constant and F_E represents the TOA radiant flux reported in the CERES library. The resulting 2D temperature distribution is illustrated in Fig. 2 as function of the spherical coordinates, considering the original data resolution.

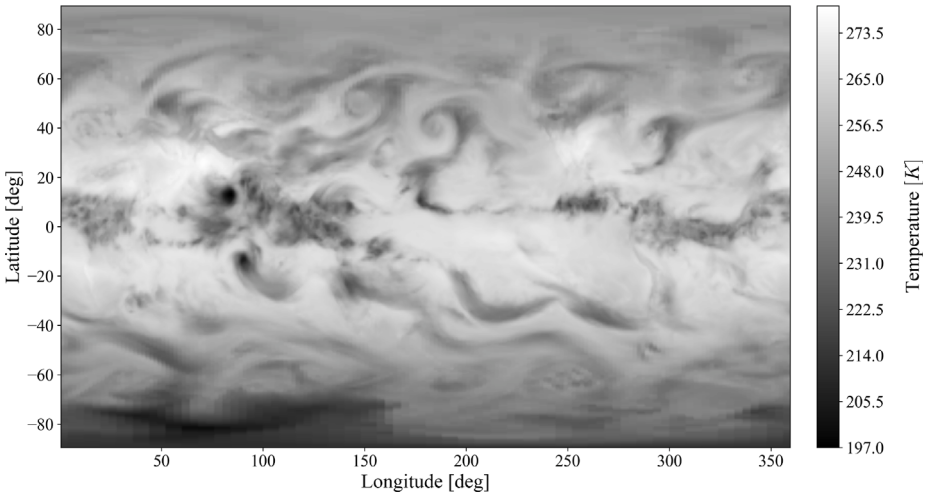

Fig. 2. TOA temperature map.

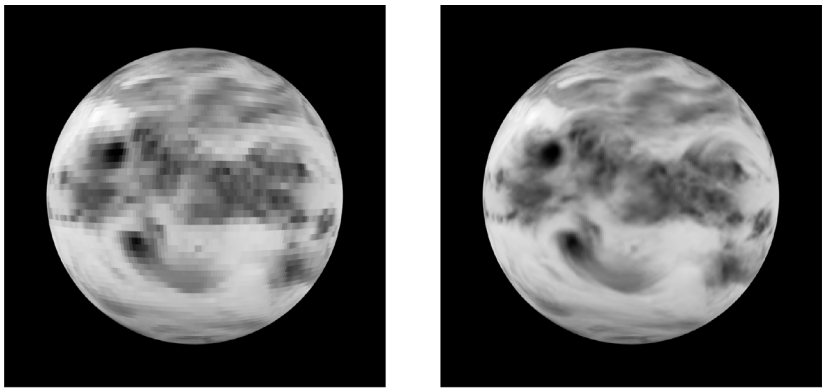

(a) Resolution: 1°. (b) Resolution: 0.1°.

Fig. 3. Temperature field of the Earth for different mesh resolutions captured with auto-span radiance scale.

Given the actual Earth's dimensions, a coarse mesh of 1° resolution would result in an extremely low resolution image, as observed in Fig. 3(a). Hence, a mesh refinement at 0.1° resolution is considered along both latitude and longitude, as illustrated in Fig. 3(b), at the expense of increased computational time. Since the computed temperatures are defined for a smaller number of gridded locations compared to the newly defined mesh, an interpolation procedure is required to characterize the temperature associated to each of the new grid element. Fig. 3 provides a visual comparison of the temperature maps before and after the refinement process, demonstrating that the results obtained with a finer mesh lead to a more realistic output.

To generate a final dataset covering a wide range of illumination conditions, eclipse scenarios are also included. After the analysis of the hourly data collected over a 24-hour interval, the daily average variation in TOA fluxes is used as a scaling factor to uniformly reduce the original radiation distribution defined under sunlight conditions. The resulting scaled radiance distribution is used to compute the corresponding eclipse temperature field according to Eq. (10), which is finally exploited to reconstruct the detected radiation, following the procedure presented in Section 3.1.

3.3. Camera noise characterization

In practical scenarios, several noise sources affect the signal detected by the thermal sensor, reducing the image quality and the accuracy of the measured parameters. As outlined in [38], uncooled microbolometer arrays are influenced by fundamental disturbances including Johnson noise, Flicker noise, and temperature fluctuation noise.

Johnson noise. Johnson noise, commonly known as thermal noise, originates from the random fluctuation of charge carriers in the resistor. The RMS voltage over the noise effective bandwidth Δf_J is reported in Eq. (11) [38], where k_B is the Boltzmann's constant, T_B is the detector temperature, and R_B is its resistance. For microbolometer using a continuous bias, the noise effective bandwidth can be determined as function of the response time constant as $\Delta f_J = (2\tau)^{-1}$.

$$v_J^{RMS} = \sqrt{4k_B T_B R_B \Delta f_J} \tag{11}$$

Flicker noise. Flicker noise, or pink noise, is another disturbance that characterizes electric circuits. It arises from the stochastic motion of photons within the detector area, resulting in fluctuations in either current or voltage. The RMS voltage decays as $1/f$, making the pink noise dominant at low frequencies. This parameter is described by Eq. (12) [38], where v_{bias} is the operating bias voltage of the detector, and $\mathcal{N}$ is the material constant associated with the resistor and the electrical circuit geometry, which can be estimated according to the Hooge empirical formula reported in [39].

$$v_{1/f}^{RMS} = v_{bias}\sqrt{\frac{\mathcal{N}}{f}} \tag{12}$$

Given a specific working frequency with low-frequency noise f_L and high-frequency noise f_H, Eq. (12) can be rewritten as Eq. (13) [38],

Table 1
Parameters and coefficients of the microbolometer [41,42].

Parameter	Symbol	Units	Value
Bolometer temperature	T_B	K	300
Bolometer resistance	R_B	kΩ	20
Detector heat conductance	G_{th}	μW K^{-1}	20
Thermal coefficient of resistance	β	K^{-1}	0.023
Time constant	τ	ms	12
Integration time	t_{int}	μs	6
Bias voltage	v_{bias}	V	5
Lower frequency at frame rate	f_L	Hz	1
Material constant	$\mathcal{N}$	–	10^{-13}

Table 2
RMS voltages of the three primary noise sources.

v_J^{RMS}	$v_{1/f}^{RMS}$	v_{th}^{RMS}
5.394×10^{-6}	5.322×10^{-6}	2.617×10^{-6}

where the high frequency bound can be computed as function of the integration time as $f_H = (2t_{int})^{-1}$, and f_L is a specification of the selected microbolometer.

$$v_{1/f}^{RMS} = v_{bias}\sqrt{\mathcal{N}\ ln\left(\frac{f_H}{f_L}\right)} \tag{13}$$

Temperature fluctuation noise. The heat exchange between the detector and its surrounding environment results in temperature fluctuation of statistical nature. The RMS voltage of this random process can be effectively described by Eq. (14) [40], where G_{th} is the heat conductance of the detector, β is the thermal coefficient of resistance, and $\Delta f_{th} = (4\tau)^{-1}$ is the effective frequency bandwidth [38].

$$v_{th}^{RMS} = \sqrt{\frac{4k_B T_B^2}{G_{th}} v_{bias}\beta^2 \Delta f_{th}} \tag{14}$$

As the heat losses from the microbolometer are primarily caused by radiant heat exchange, the fluctuation disturbance coincides with the background noise.

3.3.1. Numerical implementation

The parameters used to characterize the noise sources of the microbolometer are reported in Table 1, while the resulting RMS voltages are summarized in Table 2.

Among the different sources impacting the instrument performance, Johnson noise predominantly influences the sensor behaviour. This noise source is directly related to the temperature of the sensing material, hence, since no additional cooling is applied, the elevated temperature of the detector impacts its ability and precision in detecting weak signals. In contrast, temperature fluctuation noise, arising from the thermal fluctuations within the sensing element, typically exhibits a comparatively lower magnitude when compared to Johnson noise. This behaviour is also reflected in the spectral distribution of the NVD, which highlights the amount of noise affecting the circuit over a frequency band. Since the noise sources are uncorrelated, the NVD is analytically described by Eq. (15) [43]:

$$NVD = \frac{v_{tot}^{RMS}}{\Delta f} = \frac{\sqrt{(v_J^{RMS})^2 + (v_{1/f}^{RMS})^2 + (v_{th}^{RMS})^2}}{\Delta f} \tag{15}$$

By varying the frequency bandwidth, the NVD can be described through the spectral function reported in Fig. 4, where the red curve represents the mean of oscillations. At lower frequencies, the spectrum exhibits a distinct inclined slope, decreasing as $\propto 1/f$, which reflects the frequency-dependent behaviour of Flicker noise. However, as the operational frequency increases, the coloured noise is progressively overcome by the other two noise sources and the spectrum converges to a steady value in the order of 10^{-8} V Hz$^{-0.5}$. It is worth mentioning that

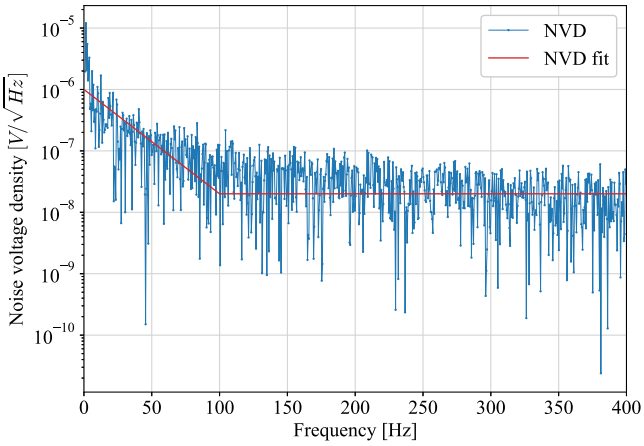

Fig. 4. NVD spectral distribution.

the noise distribution obtained with the presented analytical modelling conforms to the numerical solution outlined in literature [44,45].

To preserve a certain degree of flexibility in the rendering pipeline, the noise disturbances are added to the image during post-processing operations. Consequently, the numerical values presented in Table 2 are used to construct a two-dimensional cumulative noise distribution. Based on their inherent nature, Johnson and temperature fluctuation disturbances are modelled as white Gaussian noises with zero-mean and standard deviation equal to v_J^{RMS} and v_{th}^{RMS} respectively. In contrast, Flicker noise is modelled by low-pass filtering a white Gaussian noise with standard deviation $v_{1/f}^{RMS}$, following the formulation outlined in [11]. These separate noise maps are summed, and the resulting matrix is converted into digital units using a suitable A/D gain, established as $G_{A/D}$ =2470 ADU V^{-1} [46]. The final noise map in ADU for a given image is analytically described by Eq. (16).

$$Noise_{ADU} = G_{A/D} \cdot \left(Noise_J + Noise_{1/f} + Noise_{th}\right) \tag{16}$$

An illustrative example is reported in Fig. 5, showcasing the individual noise sources with a sample image to accentuate their disturbance. As expected, Johnson noise emerges as the most pronounced disturbance, clearly discernible in the noisy image due to its grainy texture resulting from the random variations in pixel value.

3.4. Rendering sequence

The complete rendering pipeline developed for the generation of synthetic TIR images is schematically outlined in Fig. 6, where Blender is selected as rendering software due to its high flexibility and output quality. In the context of infrared scenes, given the paramount importance of the material properties characterization, Visualization ToolKit (VTK) nodes are used to effectively read, transform, and display radiometric data obtained from thermal simulations performed using OpenFOAM. To reduce the computational effort and enhance the workflow flexibility, the thermal representations of Earth and artificial target are developed separately and subsequently merged together. While the infrared behaviour of the Earth is modelled following to the procedure presented in Section 3.2, the artificial target undergoes a thermal characterization via a 3D finite volume thermal simulation to extract the corresponding temperature distribution, as presented in [9,12]. To ensure a coherent final representation, the foreground and background levels are rendered according to a unified radiance scale, tailored based on the selected camera mode. In radiometry mode, the lower and upper bounds of the final rendering scale are determined as function of the radiant power:

$$\begin{aligned} DN_{min} = 0 \ &\rightarrow \ F_{min} = \min\{F_{target_{min}},\ F_{Earth_{min}}\} \\ DN_{max} = 2^{bit} - 1 \ &\rightarrow \ F_{max} = \max\{F_{target_{max}},\ F_{Earth_{max}}\} \end{aligned} \tag{17}$$

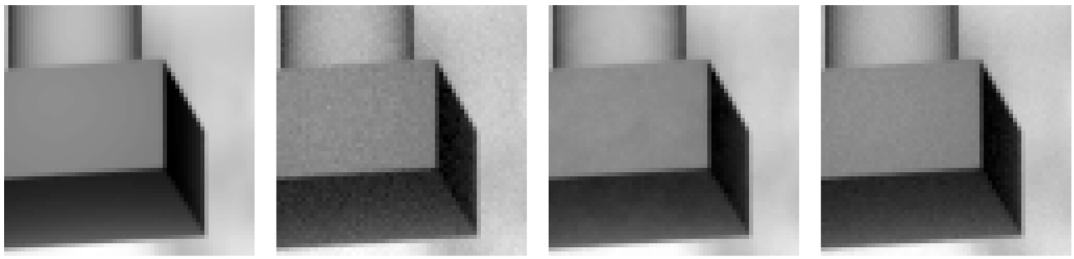

(a) Noiseless image. (b) Johnson noise. (c) Flicker noise. (d) Temperature fluctuation noise.

Fig. 5. Noise disturbance effects on zoomed portion of images.

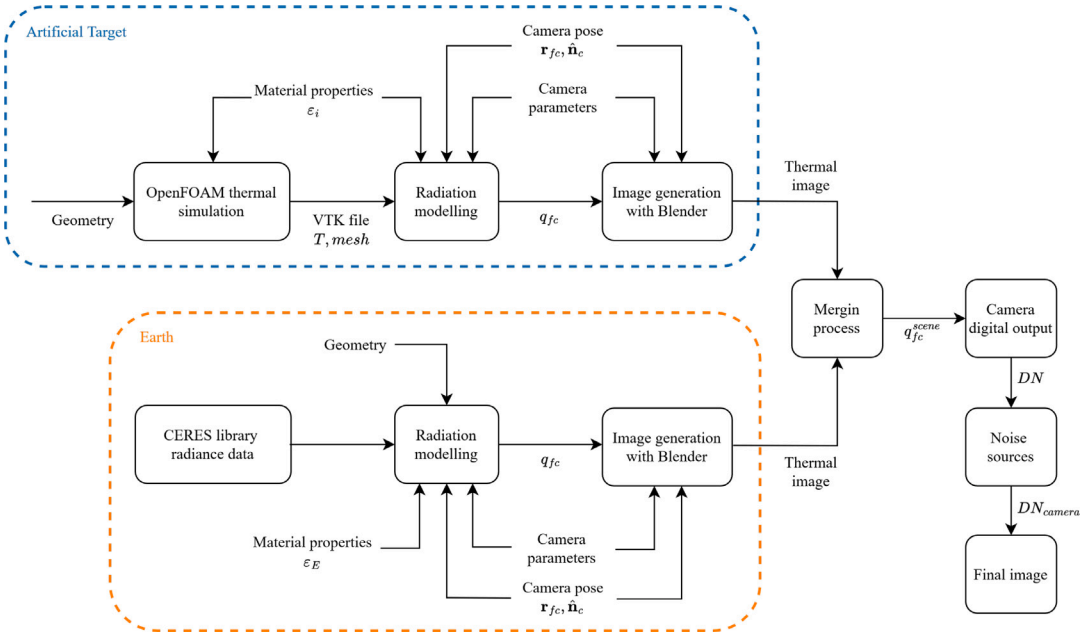

Fig. 6. Rendering sequence.

Where F_{target} and F_{Earth} are the emissive power of target and Earth, respectively. In detection mode, the digital output of the sensor, and the dynamic range of the image, are directly proportional to the radiation field intercepted by the sensor optics. Analysis of the data reveals that the detected radiation fields associated with the target and the Earth cover different orders of magnitude thus different upper bounds, as illustrated in Fig. 7.

As a consequence, the bounds of the rendering scale cannot be automatically adapted to the boundary values of the detected radiation; instead, they are set as fixed values regardless of the observed scene. This approach is necessary to maintain a sufficient contrast between the foreground and the background elements of the scene. Subsequently, the two images are generated and the fused DN map associated with the rendered image is rescaled to match the instrument response defined in Section 3.1. The final digital output of the TIR sensor, irrespectively of the camera mode selected, can be computed in ADU as reported in Eq. (18), where DN is the noiseless output described by Eqs. (5) and (9).

$$DN_{camera} = DN + Noise_{ADU} \tag{18}$$

Please note that due to the absence of coupling between raw images captured by real payloads in orbit and sensor data, the developed rendering tool has not been fully validated. However, the main sub-blocks have been compared with data found in literature, demonstrating the accuracy and coherence of the implemented models.

4. Results and analysis

4.1. Dataset generation

To focus the attention on the performance evaluation rather than on the geometrical complexity of the observed scene, a simplified geometry for the artificial target is chosen, including a cube and a cylinder. This specific selection of prisms, comprising sharp edges, plane faces and curved shapes, serves to rigorously challenge the algorithms and accentuate the visual effect caused by variations in view factor. Additionally, to capture a broader spectrum of thermal scenarios, the target is defined as a multi-material entity, with radiative properties varying throughout the simulations. Table 3 provides details of the thermal conditions imposed for the generation of the dataset.

To guarantee a correct image fusion between Earth and target representations, the spacecraft image is generated with a transparent background. Furthermore, considering the stringent on-board power requirements typical of real-world applications, the images are rendered using a monochromatic black and white colourmap, where darker shades are associated to cooler areas, and lighter regions indicate

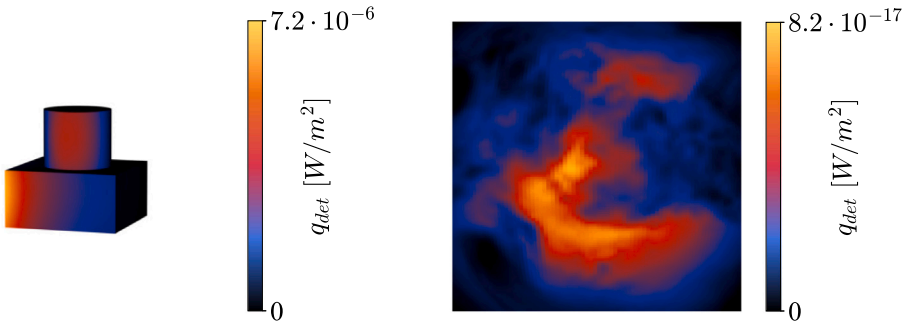

(a) Radiance flux of diffuse gray target recorded at a distance of 15 m when irradiated by the Sun.

(b) Radiance flux of Earth recorded at 4500 km from the surface when irradiated by the Sun.

Fig. 7. Measured radiance fluxes when detection mode is selected.

Table 3
Target thermal properties.

Thermal case	ϵ_{cube}	ϵ_{cyl}
Mono-material	0.86	0.86
Multi-material 1	0.90	0.10
Multi-material 2	0.10	0.90

Table 4
Camera parameters used for the image generation [33].

Parameter	Units	Value
FOV	°	16 × 12
Focal length	mm	42.2
Effective pixels	px	328 × 248
Pixel size	µm	37

Table 5
Radiance scale limits.

Case	$q_{fc_{min}}$ [W m^{-2}]	$q_{fc_{max}}$ [W m^{-2}]
Scale 1	0	$q_{fc_{max}}^{Earth} = 3 \cdot 10^{-17}$
Scale 2	0	$2 \cdot q_{fc_{max}}^{Earth} = 6 \cdot 10^{-17}$
Scale 3	0	$10 \cdot q_{fc_{max}}^{Earth} = 3 \cdot 10^{-16}$

higher radiance values. The camera parameters used in the image generation are sourced from the Hayabusa2 payload, and listed in Table 4.

The generated TIR dataset includes 12000 noisy images representing a wide range of scenarios dependent on the operative mode, illumination condition, material properties, and approach range. Concerning this latter category, both close range and far range cases are considered, with camera-spacecraft distance ranging from 15 m to 50 m, and from 340 m to 440 m respectively. The far-range interval is selected to ensure a minimum FOV coverage of 9 pixels, with the upper bound computed based on the knowledge of the IFOV and the pixel dimension and lower bound chosen to simulate an initial approach scenario. On the contrary, the camera-Earth distance is considered constant and equal to 10 871 km, corresponding to a distance from the surface of 4500 km. This specific choice results from a trade-off between the FOV coverage and the Earth mesh appearance.

Radiometry. In the radiometry branch of the dataset, since the final radiance scale is adjusted to the boundary values recorded within the scene, the images are characterized by a uniform contrast distribution, showing details associated to both the spacecraft and the Earth, as illustrated in Fig. 8. In scenarios where the target is diffused and gray, resulting in uniform emissivity across the entire body, the emissive power is sufficiently homogeneous, facilitating the discrimination of the majority of details, as reported in Fig. 8. On the contrary, in multi-material cases, concerns arise regarding the identification of the satellite under specific Earth-target-camera relative positions. Portions of the spacecraft characterized by exceedingly low emissivity (e.g. polished metal components) appear as extremely dark areas, leading to potential loss of details during target passages over the cooler areas of the background scene, corresponding to deep space or regions with minimal Earth radiation.

Detection. To assess the limitations of image processing algorithm under different radiance scale choices, the images are rendered while altering the upper bound of the rendering scale, according to the values reported in Table 5. Please note that $q_{fc_{min}}$ indicates the minimum radiance flux emitted by the scene and recorded by the camera, corresponding to the lower bound of the scale; on the contrary, $q_{fc_{max}}$ indicates the sensor maximum measurable radiance flux, corresponding to the upper bound of the rendering scale. This latter parameter is varied as function of the maximum radiant flux emitted by the Earth and received by the camera, denoted as $q_{fc_{max}}^{Earth}$. To ensure an equal comparison, for each camera pose three images are generated according to the defined scales.

Fig. 9 illustrates some examples of noisy images captured under different scale choices. Since the measured radiation associated to the target exceeds the saturation limit of the identified scales, the spacecraft always appears as a white binary map, with only its external edges distinguishable. Consequently, only the mono-material case is considered in this context. Depending on the radiance scale selected during the rendering procedure, the visibility of the Earth in the background varies. Reducing the upper bound of the scale decreases the contrast between the target and the Earth, being the latter characterized by radiance fluxes that span the entire radiance spectrum. On the contrary, by increasing the dynamic range of the image, the texture of the Earth gradually fades, eventually resulting in almost null DN values when the upper scale largely exceeds the maximum radiance emitted by the Earth. However, even with the spacecraft as the only distinguishable element in the scene, the Earth still represents an additional source of disturbance within the image for image processing algorithms.

4.2. ROI detection performance

In the context of optical navigation, image processing techniques play a crucial role in extracting effective scene information. As a consequence, the generated dataset is leveraged to assess the performance

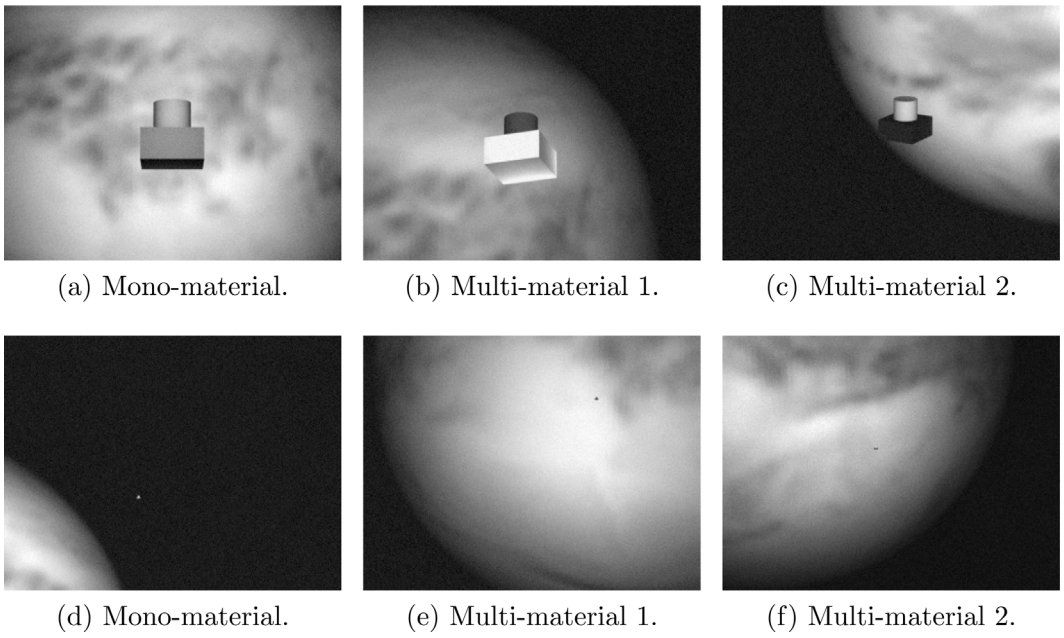

(a) Mono-material. (b) Multi-material 1. (c) Multi-material 2.

(d) Mono-material. (e) Multi-material 1. (f) Multi-material 2.

Fig. 8. TIR images generated under radiometry mode.

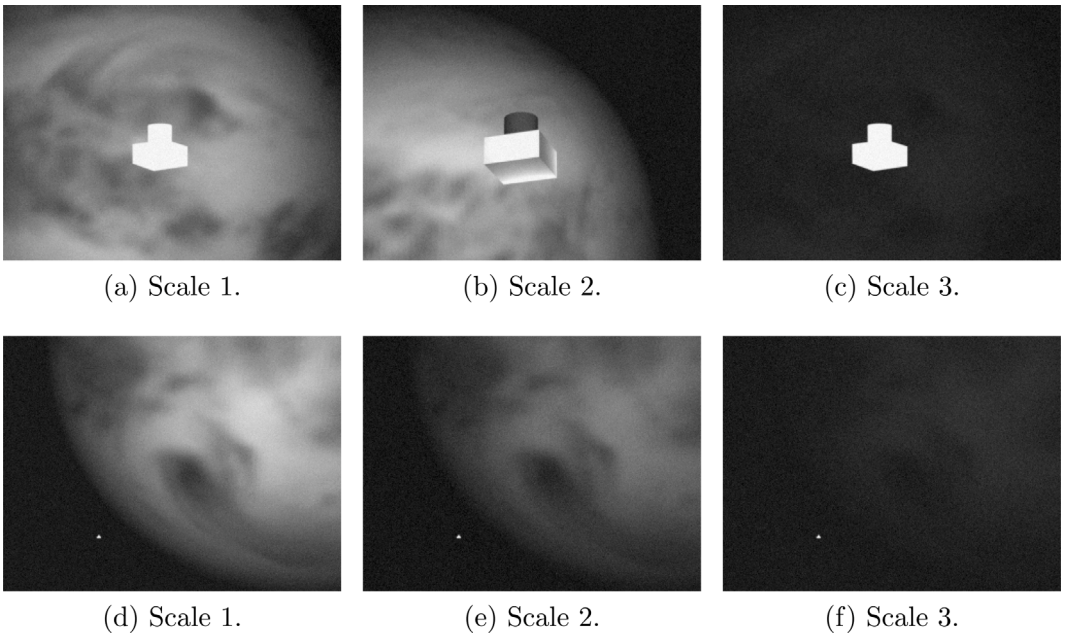

(a) Scale 1. (b) Scale 2. (c) Scale 3.

(d) Scale 1. (e) Scale 2. (f) Scale 3.

Fig. 9. TIR images generated under detection mode.

of state-of-the-art object identification algorithms, focusing on ROI detection within monocular thermal images. Since ROI detection serves as a pre-processing step to be executed onboard the spacecraft prior to the application of pose estimation algorithms for relative navigation, the selected ROI approaches must satisfy constraints in terms of memory allocation and computational time. Consequently, this work evaluates traditional methodologies, including thresholding techniques and gradient-based methodologies. The first approach is Otsu thresholding [47], which automatically selects the optimal global threshold to discriminate the foreground elements from the background by maximizing the between-class variance. A similar technique implemented is adaptive thresholding [48], where, unlike global thresholding, it computes the threshold locally for each image region, whose dimension is selected based on the trade-off between performance and computational time. A third method tested is WGE [4], which aims to isolate regions of the image characterized by stronger gradient distribution compared to weak gradient regions potentially corresponding to the background area. Lastly, DoG blob detector [49] is evaluated, whose operating principle is based on detecting the blob-like structure in the image at a specific scale depending on local maxima of the filter response. After a quick assessment of the performance of the different blob detectors, DoG is chosen as baseline as it represents the balanced trade-off between computational time and accuracy of the results. It is acknowledged that AI-based methods could also be adopted to estimate the ROI with state-of-the-art performance, as demonstrated in [3,5,50]; hence, these approaches will be further investigated in future developments. After fine-tuning the hyper-parameters to improve the performance of the individual techniques, the algorithms are evaluated based on two different metrics. Firstly, the computational time on

Table 6
Algorithms performance with radiometry data-set.

Method	Material	Mean IoU	Median IoU	Mean time [ms]
Otsu	Mono-material	0.063	0.051	0.844
	Multi-material 1	0.045	0.025	1.616
	Multi-material 2	0.028	0.022	1.274
Adaptive	Mono-material	0.806	0.916	0.754
	Multi-material 1	0.602	0.666	0.966
	Multi-material 2	0.729	0.777	0.882
WGE	Mono-material	0.822	0.897	3.940
	Multi-material 1	0.721	0.759	5.468
	Multi-material 2	0.638	0.703	5.216
Blob - DoG	Mono-material	0.150	0.150	57.436
	Multi-material 1	0.104	0.070	69.391
	Multi-material 2	0.045	0.058	60.963

CPU is assessed, and since it is measured through a Python-based algorithm implementation, it is expected that the run time will be higher compared to a C/C++ implementation scheme. Notably, testing of running time on in-flight hardware has not yet been performed at this stage of the study, but it remains a focus for future developments. The second metric is IoU [51], which quantifies the degree of overlap between the predicted bounding box and the corresponding ground truth, allowing for the discrimination between true positive detections and false positive ones.

Due to the significantly reduced performance observed under far-range scenarios owing to the limited target size, this study exclusively presents the outcomes pertaining to close-proximity conditions (from 15 m to 50 m).

Radiometry. The analysis of the average results reported in Table 6 reveals that Otsu thresholding and DoG detector consistently underperform compared to the other tested methodologies, regardless of the material distribution. This phenomenon can be attributed to the highly textured background, which challenges the fundamental assumption of these methods. Both of them rely on a global thresholding procedure, which requires the image intensity histogram to exhibit two separate classes of pixel intensity, each corresponding to a specific image level, to achieve a successful detection. However, given that both the Earth and target cover the same radiance spectrum, these findings confirm that the use of a global threshold is ineffective in scenarios characterized by limited contrast between the foreground and background of the image. Significant improvements in the results are observed with the introduction of a dynamic threshold, capable of adapting to local variations in image intensity. Adaptive thresholding consistently demonstrates superior performance of both IoU and computational time, as the more precise image segmentation process enables the preservation of edges and small-scale features. Similar results can also be reached with WGE, which leverages gradient-based discrimination. Despite the inherent flaws of TIR imaging, gradient-based solutions still offer accurate results, albeit with increased computational time, as the computed gradient exhibits similar characteristics to that of a VIS image.

The general trend presented above remains consistent even for varying camera-target distances, as illustrated in Fig. 10. As the detection range extends up to 50 m, the performance of the four methods shows a relatively stable trend, highlighting a clear difference in the outcomes achieved by Otsu and DoG compared to those of adaptive thresholding and WGE techniques.

The precision of object detection algorithms is significantly influenced by the contrast between foreground and background of the image, hence multi-material study cases pose notable challenges for all approaches, as demonstrated in Fig. 11. In the first scenario (Fig. 11(a)), although both adaptive thresholding and WGE fail in including the upper portion of the spacecraft within the ROI, they effectively detect the base of the satellite as its appearance is enhanced by the dark background, thus providing the target position estimation with an acceptable degree of accuracy. On the contrary, DoG and Otsu methods demonstrate ineffectiveness to properly identify the spacecraft, as it does not correspond to the brightest portion of the image. An analogous trend is observed in the second case (Fig. 11(b)), where the most radiative portion of the artificial object blends into the background, causing the algorithms to focus either on the brightest part of the frame, or on the dark portion of the spacecraft, which stands out against the Earth. A different outcome is observed in Fig. 11(c), where target and Earth cover sufficiently different radiance spectrum. In such cases, adaptive thresholding and WGE methods accurately detect the entire satellite, while DoG and Otsu approaches still confirm their lower performance.

Table 7
Algorithms performance with detection data-set.

Method	Material	Mean IoU	Median IoU	Mean time [ms]
Otsu	Scale 1	0.124	0.031	1.002
	Scale 2	0.576	0.867	0.337
	Scale 3	0.904	0.900	0.328
Adaptive	Scale 1	0.677	0.832	1.564
	Scale 2	0.715	0.837	0.406
	Scale 3	0.714	0.838	0.373
WGE	Scale 1	0.767	0.804	4.444
	Scale 2	0.837	0.881	4.003
	Scale 3	0.838	0.882	3.970
Blob - DoG	Scale 1	0.802	0.697	15.28
	Scale 2	0.862	0.698	13.546
	Scale 3	0.860	0.714	13.766

Detection. With reference to Table 7, it is observed that the use of Scale 1 images consistently yields sub-optimal results irrespective of methodology selected. Despite the target being represented as a white and well-defined area, the presence of saturated regions on the Earth surface notably influences the final detection outcomes, especially when highly textured backgrounds are considered. Increasing the dynamic range of the captured scene significantly enhances the average performance, as the improved contrast achieved in the images enables more effective discrimination of the target against the background. The largest improvement in detection capabilities involves methodologies based on global thresholding, with Otsu approach showing an IoU increment of 360% with halved computational time. Improvements in the runtime are recorded also for adaptive thresholding and DoG, while WGE exhibits a constant trend irrespective of the scale. The most favourable outcomes are observed with the widest dynamic range (Scale 3), where the Earth is marginally visible and its disturbance is minimized. In this scenario, the image intensity histogram is split into two separate regions, each associated with a specific image level, as illustrated in Fig. 12, greatly improving the performance of both Otsu and DoG approaches in the ROI extraction process.

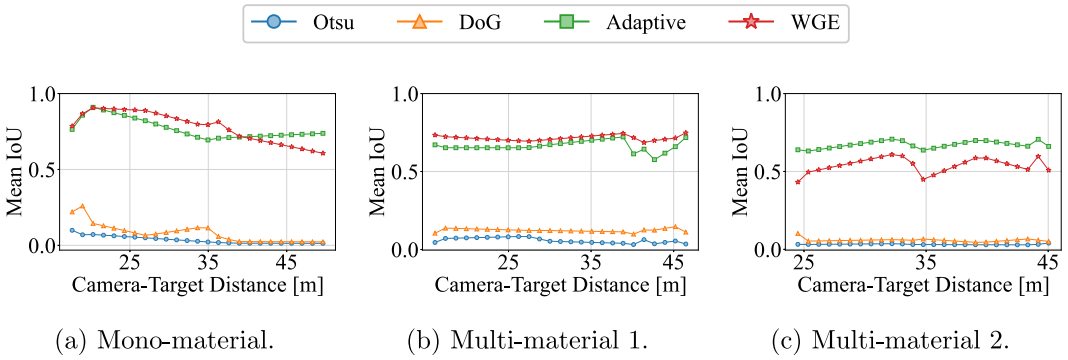

Fig. 10. IoU performance as function of the camera-target distance for different material combinations.

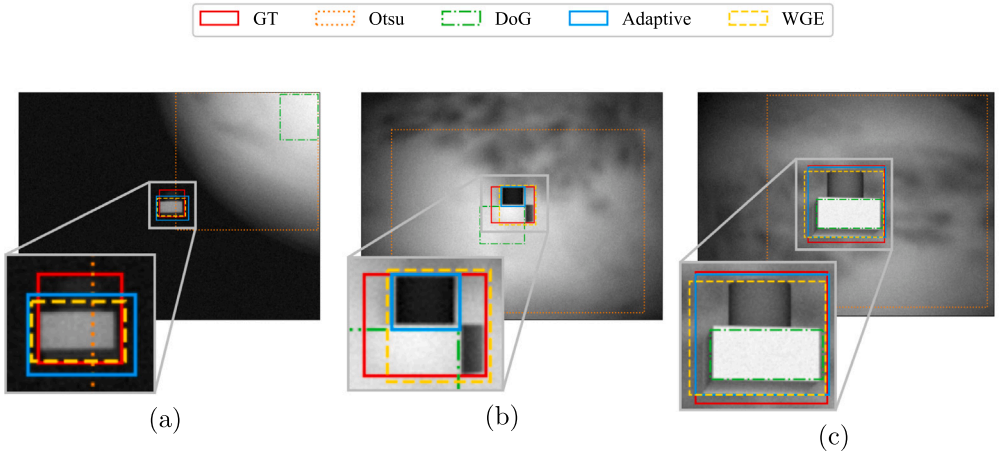

Fig. 11. ROI prediction with multi-material target.

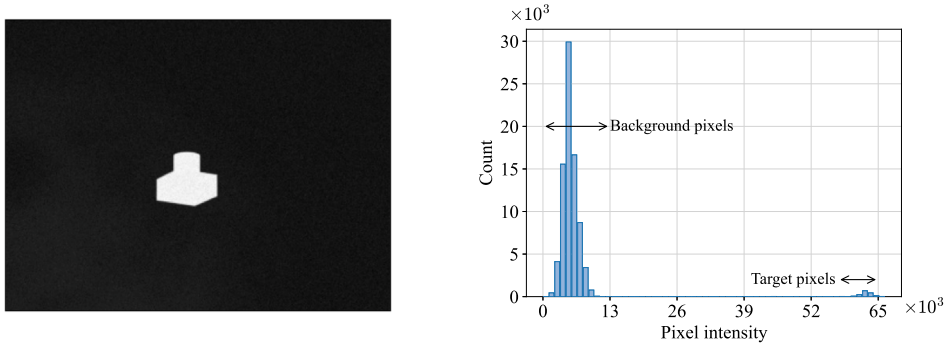

Fig. 12. Scale 3 intensity histogram.

By observing Fig. 13, it is possible to verify the data reported in Table 7, where the ROI predicted by each methodology are compared under different radiance scales. It is clearly visible how the detection capabilities of global thresholding improves with reduced Earth visibility, reaching an accuracy comparable to that of adaptive thresholding and WGE.

Analogously to the analyses performed for the radiometry branch of the dataset, the algorithms performance is evaluated as function of the camera-target distance, as shown in Fig. 14. While Scale 3 frames show minimal variation in IoU scores with increasing distance, substantial peaks are observed with Scale 1 and Scale 2 representations, as the lowest contrast of the image can yield the misclassification of the Earth as part of the background. Furthermore, it is here highlighted how the performance of Otsu thresholding further improves with increased dynamic range, granting the highest scores when Scale 3 representations are considered.

5. Case study: Tango spacecraft

Due to the satisfactory outcomes provided by state-of-the-art approaches in accurately detect a simplified spacecraft geometry, the following section is dedicated to assessing the performance of the most performant methodologies, namely adaptive thresholding and WGE

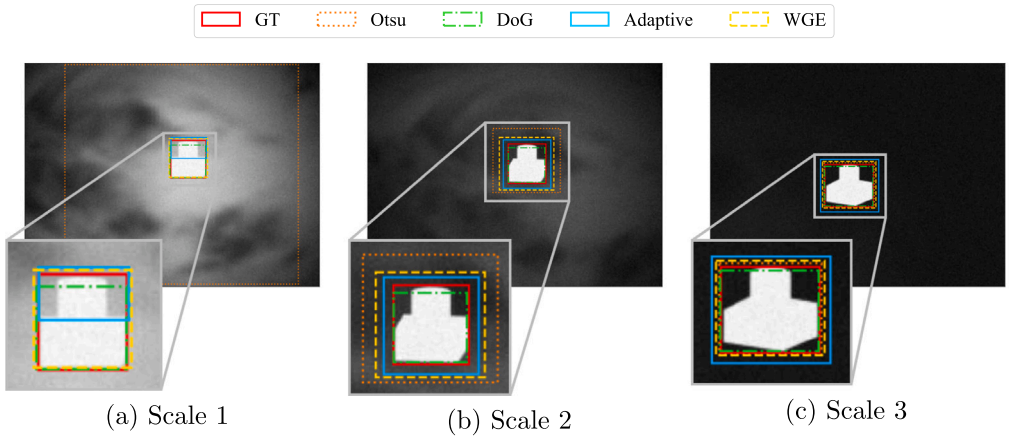

Fig. 13. ROI prediction with different radiance scale choices.

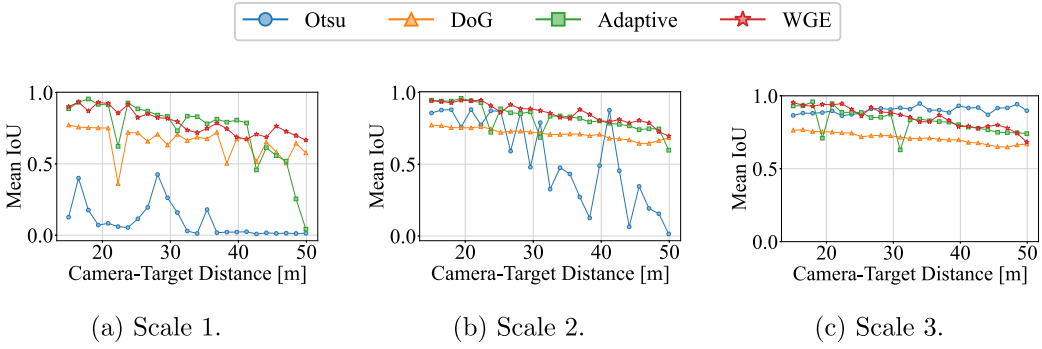

Fig. 14. IoU performance as function of the camera-target distance for different scale choices.

algorithms, to verify their robustness with a more complex satellites, both in terms of geometry and thermal properties.

The selected satellite for the case study is Tango, the target spacecraft in the Swedish-led PRISMA mission [14]. Given the lack of publicly available thermal images for the selected spacecraft, a custom dataset of 1000 noisy images of Tango is generated in radiometric mode by exploiting the rendering pipeline presented in this paper. The unavailability of an official CAD model of the satellite necessitates the development of a simplified yet representative one based on the dimensions of its main components reported in [4]. The thermal properties are derived from the implementation of a multi-material thermal simulation, where each system component is assigned the corresponding radiative and thermophysical properties. However, the assumption of graybody Lambertian emitter still applies.

Examples of synthetic images of Tango rendered under close-range scenarios are shown in Fig. 15. While the rendering technique is the same used to generate the simplified dataset illustrated in Section 4, the geometrical and thermal properties of the Tango are significantly more complex compared to the prism used to evaluate the performance of traditional ROI detection algorithms. As a consequence, the resulting images show a different contrast distribution between Earth and satellite, representing a more realistic scenario.

5.1. ROI detection performance

The analysis of the radiative heat flux emitted by Tango and intercepted by the camera reveals that the radiation spectrum covered is broader compared to that of the Earth. Under camera detection mode, this results in images characterized by a uniform white region representative of Tango against a background of variable intensity, similarly to the representations reported in Fig. 9. As a consequence, it is expected that the results presented in Table 7 will hold true also for a more complex geometry, and the following ROI detection analysis only relies on the radiometry dataset of Tango spacecraft.

Table 8
Algorithms performance with radiometry data-set of Tango spacecraft.

Method	Mean IoU	Median IoU	Mean time [ms]
Adaptive	0.625	0.705	1.217
WGE	0.393	0.161	6.123

Table 8 reports the median IoU score and the mean computational time achieved by adaptive thresholding and WGE algorithms. The general trend of adaptive thresholding mirrors the one presented in Table 6 for the simplified multi-material target, demonstrating its robustness when faced with complex geometries and different material distributions. By observing the images reported in Fig. 16 it can be noticed how the intrinsic nature of adaptive thresholding allows it to adjust to the unique characteristics of each image, enabling an accurate detection with different backgrounds. On the contrary, WGE encounters significant challenges during the detection process, reaching an average score of just 0.2. Due to the heterogeneous thermal properties of Tango, its gradient distribution can be hardly distinguished from the Earth contribution, as reported in Fig. 17, and since the algorithm employs a fixed threshold for gradient discrimination rather than a variable one, it struggles in identifying the target. By focusing the attention on Fig. 16(a) and its corresponding gradient distribution (Fig. 17(a)), it can be observed that there is not a clear distinction between the gradient of the Earth and the one associated to the target, thus misleading the detection process and including part of the background into the

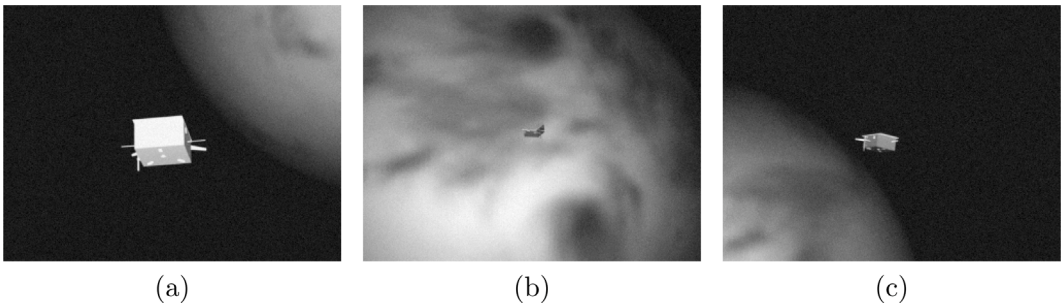

Fig. 15. Tango TIR images generated following the presented methodology under radiometry mode.

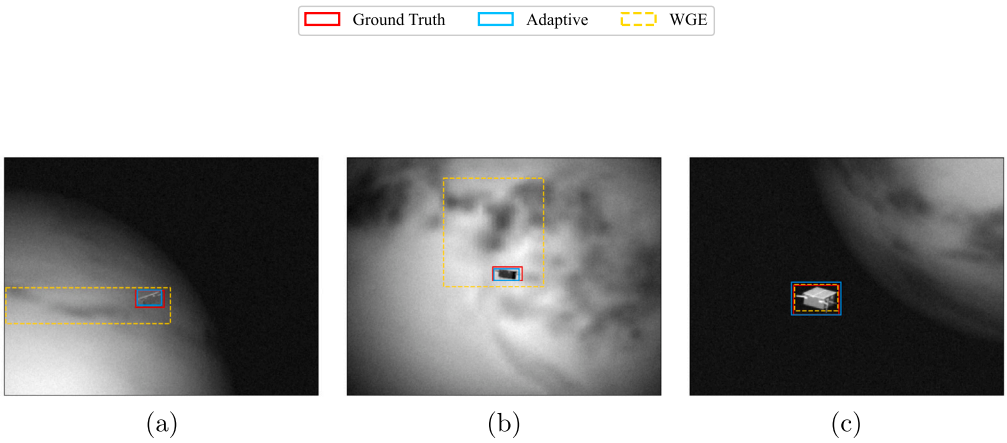

Fig. 16. ROI detection with Tango.

bounding box. A different scenario is observed in Fig. 16(b) and the corresponding gradient in Fig. 17(b). Here the gradient associated to the front face of Tango is characterized by a higher contribution with respect to the background, aiding the algorithm in the identification of the target. Yet, the use of a fixed gradient threshold leads to the erroneous detection of the highly-textured portion of the Earth, which is characterized by a higher contrast distribution. Better results are visible in Fig. 16(c), where the satellite emits a radiative flux higher with respect to that of the Earth, yielding a more pronounced gradient distribution. In this case, WGE is able to accurately detect the target with an accuracy of IoU=0.80, comparable to the 0.83 score reached by adaptive thresholding.

Tables 6 and 8 highlight the significant difference in performance of the WGE algorithm when applied to the simplified multi-material target and the Tango spacecraft. In the simplified case, the target consists of only two materials, and despite one of them having a low emissivity, hence appearing as a dark blob and blending with the background, the higher emissivity of the remainder of the spacecraft allows the algorithm to detect the target, as it appears brighter compared to the rest of the scene. However, this is not the case of the Tango spacecraft, whose heterogeneous thermal properties and a more complex geometry make accurate detection more challenging. As a consequence, the simplified test case presented in the previous sections is based on overly stringent assumptions, necessitating a refinement of the model.

In the final analysis, the robustness of WGE algorithm is compromised when confronted with a wide spectrum of material combinations and highly textured backgrounds, whereas adaptive thresholding, thanks to its flexibility, proves better suited for applications to diverse scenarios as the one included in the generated dataset.

6. Conclusions and future works

The work presented in this article highlighted the necessity of investigating the potential of monocular thermal imaging for navigation purposes. Prior to the direct application of navigation algorithms, a pre-processing step is implemented, evaluating the performance of state-of-the-art computer vision methodologies with the focus on object detection when a low-Earth environment is encountered. This issue is firstly addressed by generating a dataset of spaceborne scenarios through the implementation of a rendering pipeline that accounts for the properties of the thermal camera and its main noise sources, and for the physical interpretation of the radiative heat exchange between the sensor and the observed scene. The background of the generated images includes the Earth, whose model is based on satellite-based measurements collected in the CERES database, which allow to model its infrared behaviour while reducing the computational burden required for the rendering process. The resulting synthetic images have been leveraged to evaluate the performance of ROI detection algorithms. The analysis of both thresholding techniques and gradient-based methodologies highlighted the influence of camera mode, material combinations, dynamic range, and presence of the textured backgrounds on the detection accuracy. Despite the simplified target geometry, the analyses performed for the radiometry mode show that adaptive thresholding and WGE demonstrate promising results in mitigating the influence of the Earth in the ROI extraction process, reaching mean scores up to 0.91 and 0.89, respectively, while maintaining computational times in the order of few milliseconds. The inclusion of multi-material targets revealed how low emissivity portions of the spacecraft can affect the detection capabilities, especially in correspondence of cooler background regions, leading to decrements in the performance of 22% for WGE. The analyses performed on the detection dataset confirm the superior performance of adaptive thresholding and WGE, while concurrently revealing a large performance increment for DoG detector, reaching IoU

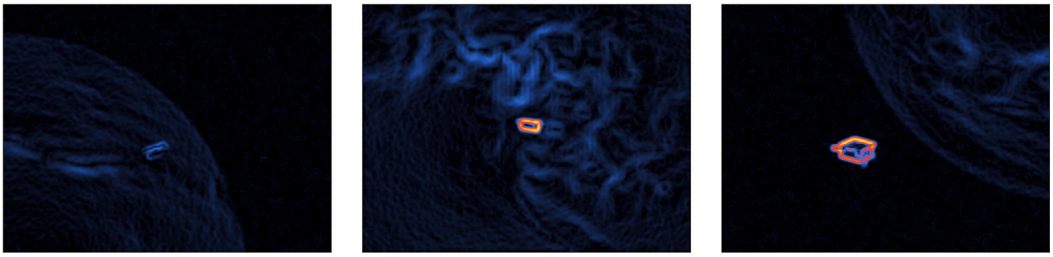

Fig. 17. Gradient distribution of the Tango images reported in Fig. 16.

values of 0.6. The enlargement of the dynamic range of the image scale results in extremely high-contrast images, yielding higher scores for all the evaluated methodologies. Yet, adaptive thresholding and WGE still prove the most suited algorithms irrespectively of the selected scale. As a consequence, these two algorithms have also been tested on a set of TIR images representative of the test case of Tango spacecraft under radiometry scenarios. The increased geometrical complexity entails a decrement in performance compared to the simplified spacecraft scenario, showing a big shift in performance of the WGE. On the contrary, adaptive thresholding still reaches an average IoU of 0.705, thus providing satisfactory detection accuracy. The results derived from the proposed analyses confirm the possibility of exploiting monocular thermal imaging for autonomous close-proximity operations, yet an intensive algorithm testing campaign shall be performed on a more comprehensive dataset of images.

6.1. Future developments

The future developments may focus on the improvement of the geometrical model of the target, along with the validation of the rendering pipeline developed. Conducting a validation campaign with a flight hardware is fundamental to verify the accuracy of the implemented model and enhance the fidelity of the generated outcomes. However, this implies the development of an adequate facility representative of the space environment, which poses significant challenges particularly regarding the thermal control of the scene. It could be also interesting to evaluate the performance of machine learning algorithms. Leveraging the promising results already demonstrated in the VIS spectrum, AI-based techniques could aid in identifying and learning distinctive target features and surface thermal properties, refining the detection area and yielding a more robust architecture. To enhance the adaptability of the process and develop an algorithm that perform well regardless of the selected spectral band, the network can be trained and tested on a mixed dataset including VIS, TIR and VIS-TIR fused images. This approach would also optimize the computational resources and simplify the pipeline for processing multi-spectral images. Additionally, hardware-in-the-loop activities can be performed to integrate the developed algorithms with in-flight hardware components and optimize the selected procedures to meet memory requirements.

CRediT authorship contribution statement

Lucia Bianchi: Writing – original draft, Visualization, Software, Resources, Methodology, Investigation, Formal analysis, Data curation, Conceptualization. **Michele Bechini:** Writing – review & editing, Visualization, Methodology, Formal analysis, Conceptualization. **Matteo Quirino:** Writing – review & editing, Visualization, Methodology, Formal analysis, Conceptualization. **Michèle Lavagna:** Writing – review & editing, Supervision, Conceptualization.

Declaration of competing interest

The authors declare that they have no known competing financial interests or personal relationships that could have appeared to influence the work reported in this paper.

References

[1] J. Jiang, X. Chen, W. Dai, Z. Gao, Y. Zhang, Thermal-inertial SLAM for the environments with challenging illumination, IEEE Robot. Autom. Lett. 7 (4) (2022) 8767–8774, http://dx.doi.org/10.1109/LRA.2022.3185385.

[2] M. Bass, E.W.V. Stryland, D.R. Williams, W.L. Wolfe, Handbook of optics, second ed., McGraw-Hill, 1995, pp. 1–1664.

[3] M. Piazza, M. Maestrini, P. Di Lizia, Monocular relative pose estimation pipeline for uncooperative resident space objects, J. Aerosp. Inf. Syst. 19 (9) (2022) 613–632, http://dx.doi.org/10.2514/1.I011064.

[4] S. Sharma, J. Ventura, S. D'Amico, Robust model-based monocular pose initialization for noncooperative spacecraft rendezvous, AIAA J. Spacecr. Rockets 55 (6) (2018) 1414–1429, http://dx.doi.org/10.2514/1.A34124.

[5] M. Bechini, G. Gu, P. Lunghi, M. Lavagna, Robust spacecraft relative pose estimation via CNN-aided line segments detection in monocular images, Acta Astronaut. 215 (2024) 20–43, http://dx.doi.org/10.1016/j.actaastro.2023.11.049.

[6] M. Bechini, M. Lavagna, P. Lunghi, Dataset generation and validation for spacecraft pose estimation via monocular images processing, Acta Astronaut. 204 (2023) 358–369, http://dx.doi.org/10.1016/j.actaastro.2023.01.012, URL https://www.sciencedirect.com/science/article/pii/S0094576523000127.

[7] O.B. Yilmaz, N. Aouf, L. Majewski, M. Sánchez-Gestido, G. Ortega, Using infrared based relative navigation for active debris removal, in: 10th International ESA Conference on Guidance, Navigation, and Control Systems, 2017, URL https://api.semanticscholar.org/CorpusID:56418626.

[8] L. Pasqualetto Cassinis, R. Fonod, E. Gill, Review of the robustness and applicability of monocular pose estimation systems for relative navigation with an uncooperative spacecraft, Prog. Aerosp. Sci. (2019) http://dx.doi.org/10.1016/j.paerosci.2019.05.008.

[9] M. Quirino, Novel Thermal Images Generator for Autonomous Space Proximity Operations (Ph.D. thesis), Politecnico di Milano, 2023, URL https://www.politesi.polimi.it/handle/10589/213812.

[10] M. Quirino, M.R. Lavagna, Spacecraft and asteroid thermal image generation for proximity navigation and detection scenarios, Appl. Sci. 14 (13) (2024) http://dx.doi.org/10.3390/app14135377, URL https://www.mdpi.com/2076-3417/14/13/5377.

[11] G.L. Civardi, M. Bechini, M. Quirino, A. Colombo, M. Piccinin, M. Lavagna, Generation of fused visible and thermal-infrared images for uncooperative spacecraft proximity navigation, Adv. Space Res. (2023) http://dx.doi.org/10.1016/j.asr.2023.03.022, URL https://www.sciencedirect.com/science/article/pii/S0273117723002144.

[12] M. Quirino, L. Marocco, M. Guilizzoni, M. Lavagna, High energy rapid modular ensemble of satellites payload thermal analysis using openFOAM, J. Thermophys. Heat Transf. 35 (2021) http://dx.doi.org/10.2514/1.T6165.

[13] NASA, CERES project, 1997, URL https://ceres.larc.nasa.gov/ (Accessed: 17 May 2023).

[14] M. D'Errico, Distributed space missions for earth system monitoring, Space Technology Library, Springer New York, 2013, pp. 599–637.

[15] T. Okada, T. Fukuhara, M. Taguchi, T. Arai, T. Imamura, H. Senshu, T. Sekiguchi, Y. Ogawa, H. Demura, N. Sakatani, Y. Horikawa, J. Helbert, T. Mueller, A. Hagermann, Thermal infrared imager TIR on Hayabusa2: Result of ground calibration, in: Asteroids, Comets, Meteors, Helsinki, 2014, URL https://www.researchgate.net/publication/275582834.

[16] B. Cavrois, A. Vergnol, A. Donnard, P. Casiez, O. Mongrard, LIRIS demonstrator on ATV5: a step beyond for European non cooperative navigation system, in: AIAA Guidance, Navigation, and Control Conference, http://dx.doi.org/10.2514/6.2015-0336, arXiv:https://arc.aiaa.org/doi/pdf/10.2514/6.2015-0336.

[17] J.M. Galante, J.V. Eepoel, C. D'souza, B. Patrick, Fast Kalman filtering for relative spacecraft position and attitude estimation for the raven ISS hosted payload, 2016, URL https://api.semanticscholar.org/CorpusID:49392606.
[18] S. Sharma, S. D'Amico, Neural network-based pose estimation for noncooperative spacecraft rendezvous, IEEE Trans. Aerosp. Electron. Syst. 56 (6) (2020) 4638–4658, http://dx.doi.org/10.1109/TAES.2020.2999148.
[19] V. Capuano, S.R. Alimo, A.Q. Ho, S.J. Chung, Robust feature extraction for on-board monocular-based spacecraft pose acquisition, in: AIAA Scitech 2019 Forum, American Institute of Aeronautics and Astronautics Inc, AIAA, 2019, http://dx.doi.org/10.2514/6.2019-2005.
[20] T.H. Park, S. Sharma, S. D'Amico, Towards robust learning-based pose estimation of noncooperative spacecraft, 2019, CoRR arXiv:1909.00392.
[21] M. Bechini, G.L. Civardi, M. Quirino, A. Colombo, M. Lavagna, Robust monocular pose initialization via visual and thermal image fusion, in: 73rd International Astronautical Congress, IAC, 2022.
[22] J.-F. Shi, S. Ulrich, Uncooperative spacecraft pose estimation using monocular monochromatic images, J. Spacecr. Rockets 58 (2) (2021) 284–301, http://dx.doi.org/10.2514/1.A34775, arXiv:10.2514/1.A34775.
[23] M. Bechini, Monocular vision for uncooperative targets through AI-based methods and sensor fusion, (Ph.D. thesis), Politecnico di Milano, 2024, URL https://www.politesi.polimi.it/handle/10589/216793.
[24] F. Schnitzer, A. Sonnenburg, K. Janschek, M. Gestido, Lessons-learned from on-ground testing of image-based non-cooperative rendezvous navigation with visible-spectrum and thermal infrared cameras, in: 10th International ESA Conference on Guidance, Navigation & Control Systems, 2017.
[25] D. Mora, M. Avilés, M. Canetri, P. Colmenarejo, A complete IP-based navigation solution for the approach and capture of active debris, in: 67th International Astronautical Congress, IAC, 2016, URL https://www.researchgate.net/publication/320281011.
[26] J. Tao, Y. Cao, M. Ding, Z. Zhang, Visible and infrared image fusion-based image quality enhancement with applications to space debris on-orbit surveillance, Int. J. Aerosp. Eng. 2022 (2022) http://dx.doi.org/10.1155/2022/6300437.
[27] Himawari-8/9 Himawari Standard Data User's Guide, first ed., Japan Meteorological Agency, 1-3-4 Otemachi, Chiyoda-ku, Tokyo, 100-8122 Japan, 2017.
[28] M. Vollmer, M. Klaus-Peter, Infrared Thermal Imaging: Fundamentals, Research and Applications, first ed., John Wiley & Sons, Inc., 2011, pp. 1–593.
[29] E. Brageot, O. Groussin, P. Lamy, J.L. Reynaud, Experimental study of an uncooled microbolometer array for thermal mapping and spectroscopy of asteroids, Exp. Astron. 38 (2014) 381–400, http://dx.doi.org/10.1007/s10686-014-9417-y.
[30] F. Capaccioni, A. Coradini, et al., The organic-rich surface of comet 67P/Churyumov-Gerasimenko as seen by VIRTIS/Rosetta, Sciene 347 (2015) http://dx.doi.org/10.1126/science.aaa0628, URL www.sciencemag.org.
[31] A. Maturilli, J. Helbert, H. Hiesinger, M. D'Amore, MERTIS on BepiColombo cruise operations: flybys to the moon and venus, in: 52nd Lunar and Planetary Science Conference, 2021, Berlin.
[32] J.H. Lienhard IV, J.H. Lienhard, A Heat Transfer Textbook, fifth ed., Dover Publications, Mineola, NY, 2019, URL http://ahtt.mit.edu.
[33] T. Okada, T. Fukuhara, S. Tanaka, M. Taguchi, T. Imamura, T. Arai, H. Senshu, Y. Ogawa, H. Demura, K. Kitazato, R. Nakamura, T. Kouyama, T. Sekiguchi, S. Hasegawa, T. Matsunaga, T. Wada, J. Takita, N. Sakatani, Y. Horikawa, K. Endo, J. Helbert, T.G. Müller, A. Hagermann, Thermal infrared imaging experiments of C-type asteroid 162173 ryugu on Hayabusa2, Space Sci. Rev. 208 (2017) 255–286, http://dx.doi.org/10.1007/s11214-016-0286-8.
[34] T. Arai, T. Nakamura, S. Tanaka, H. Demura, Y. Ogawa, N. Sakatani, Y. Horikawa, H. Senshu, T. Fukuhara, T. Okada, Thermal imaging performance of TIR onboard the hayabusa2 spacecraft, Space Sci. Rev. 208 (2017) 239–254, http://dx.doi.org/10.1007/s11214-017-0353-9.
[35] P.W. Nugent, J.A. Shaw, Calibration of uncooled LWIR microbolometer imagers to enable long-term field deployment, in: The International Society for Optical Engineering, vol. 9071, SPIE, 2014, http://dx.doi.org/10.1117/12.2053082.
[36] G. Matthews, Celestial body irradiance determination from an underfilled satellite radiometer: application to albedo and thermal emission measurements of the moon using CERES, Appl. Opt. 47 (27) (2008) 4981–4993, http://dx.doi.org/10.1364/AO.47.004981.
[37] Q. Fu, K.N. Liou, LaFuLi: NASA langley Fu-Liou radiative transfer code, 2021, ascl:2104.008, arXiv:2104.008.
[38] Y. tang Gao, H. min Chen, Y. Xu, X. nan Sun, B. kang Chang, Noise research of microbolometer array under temperature environment, in: International Symposium on Photoelectronic Detection and Imaging 2011: Advances in Infrared Imaging and Applications, vol. 8193, SPIE, 2011, p. 81930S, http://dx.doi.org/10.1117/12.899421.
[39] F. Hooge, 1/F noise is no surface effect, Phys. Lett. A 29 (3) (1969) 139–140, http://dx.doi.org/10.1016/0375-9601(69)90076-0, URL https://www.sciencedirect.com/science/article/pii/0375960169900760.
[40] W.A. Lentz, Characterization of noise in uncooled IR bolometer arrays, Massachusetts Institute of Technology, Cambridge, MA, 1998.
[41] C. Ringqvist, G. Mele, H. akan Carlsson, J. Karlsson, M.B. Syberg, O. Runborg, P. Enqvist, U.W. allgren, FLIR project-modeling noise in bolometer signal, 2018, URL https://www.scienceabc.com/.
[42] M. Liger, Uncooled carbon microbolometer imager, 2006.
[43] D. Fitzpatrick, Analog Design and Simulation Using OrCAD Capture and PSpice, second ed., Newnes, 2018, pp. 197–208, http://dx.doi.org/10.1016/B978-0-08-102505-5.00014-8, URL https://www.sciencedirect.com/science/article/pii/B9780081025055000148.
[44] N. Shen, J. Yu, Z. Tang, An uncooled infrared microbolometer array for low-cost applications, IEEE Photonics Technol. Lett. 27 (2015) 1247–1249, URL https://api.semanticscholar.org/CorpusID:22575631.
[45] S. Eminoglu, M. Tanrikulu, T. Akin, A low-cost 128x128 uncooled infrared detector array in CMOS process, J. Microelectromech. Syst. 17 (2008) 20–30, http://dx.doi.org/10.1109/JMEMS.2007.910235.
[46] I. Sedgwick, S. Benhammadi, N. Guerrini, B. Marsh, Development of low noise pixels and readout architectures for scientific applications in a 180 nm CMOS image sensor process, J. Instrum. 17 (2022) http://dx.doi.org/10.1088/1748-0221/17/11/C11007.
[47] N. Otsu, Threshold selection method from gray-level histograms, IEEE Trans. Syst. Man Cybern. 9 (1979) 62–66, http://dx.doi.org/10.1109/TSMC.1979.4310076, URL https://ieeexplore.ieee.org/document/4310076.
[48] J. Gauci, O. Falzon, C. Formosa, A. Gatt, C. Ellul, S. Mizzi, A. Mizzi, C.S. Delia, K. Cassar, N. Chockalingam, K.P. Camilleri, Automated region extraction from thermal images for peripheral vascular disease monitoring, J. Healthcare Eng. 2018 (2018) http://dx.doi.org/10.1155/2018/5092064.
[49] D.G. Lowe, Distinctive image features from scale-invariant keypoints, Int. J. Comput. Vis. 60 (2004) 91–110, http://dx.doi.org/10.1023/B:VISI.0000029664.99615.94.
[50] L. Pauly, W. Rharbaoui, C. Shneider, A. Rathinam, V. Gaudillière, D. Aouada, A survey on deep learning-based monocular spacecraft pose estimation: Current state, limitations and prospects, Acta Astronaut. 212 (2023) 339–360, http://dx.doi.org/10.1016/j.actaastro.2023.08.001, URL https://www.sciencedirect.com/science/article/pii/S0094576523003995.
[51] M. Goyal, M.H. Yap, S. Hassanpour, Region of interest detection in dermoscopic images for data-augmentation, 2018, ArXiv URL http://arxiv.org/abs/1807.10711.